1990-01

Numerical simulation of the effects of variation of angle of attack and sweep angle on vortex breakdown over delta wings

Ekaterinaris, J.A.; Schiff, Lewis B.

AIAA-90-3000-CP

Numerical Simulation of the Effects of Variation of Angle of Attack and Sweep Angle on Vortex Breakdown over Delta Wings

J. A. Ekaterinaris*
Navy–NASA Joint Institute of Aeronautics
NASA Ames Research Center, Moffett Field CA, 94035

and

Lewis B. Schiff†
NASA Ames Research Center, Moffett Field CA, 94035

Abstract

The structure of the vortical flowfield over delta wings at high angles of attack was investigated. Three–dimensional Navier–Stokes numerical simulations were carried out to predict the complex leeward–side flowfield characteristics, including leading edge separation, secondary separation, and vortex breakdown. Flows over a 75° and a 63° sweep delta wing with sharp leading edges were investigated and compared with available experimental data. The effect of variation of circumferential grid resolution in the vicinity of the wing leading edge on the accuracy of the solutions was addressed. Further, the effect of turbulence modeling on the solutions was investigated. The effects of variation of angle of attack on the computed vortical flow structure for the 75° sweep delta wing were examined. At moderate angles of attack no vortex breakdown was observed. When a critical angle of attack was reached, bubble–type vortex breakdown was found. With further increase in angle of attack, a change from bubble–type breakdown to spiral–type vortex breakdown was predicted by the numerical solution. The effects of variation of sweep angle and free–stream Mach number were addressed with the solutions on a 63° sweep delta wing.

Introduction

Characteristic of the flow over a delta wing at an angle of attack is the occurrence of the leeward–side vortices resulting from the separation of the windward and leeward side boundary layers from the leading edge. The separated boundary layers, or detached shear layers, roll up to form the primary leading–edge vortices. The intersection of the vortex feeding sheets with a plane normal to the wing surface shows a spiraling pattern. Velocity profiles in the inner portion of this spiral appear to be nearly axisymmetric. The vortical region grows in size and strength along the body. If the primary vortices are strong enough, then secondary separations and secondary vortices are observed under the primary vortices inboard of the leading edge. The energetic character of the leeward side vortical flowfield provides additional vortical lift, which has been successfully utilized in modern aircraft.

As the angle of attack increases, the leeward–side leading edge–vortices are strengthened, and the lift of the delta wing increases. When a critical angle of attack is reached, bursting of the vortices occurs and the structure of the flowfield changes dramatically. At the bursting point the velocity in a particular streamline may stagnate. Downstream of the stagnation point, reversed axial velocities are observed, and the breakdown is usually followed by a turbulent wake. Breakdown has adverse effects on the lifting characteristics of the wing, and may be the source of a large–scale unsteady flow. Understanding the mechanisms which generate vortex breakdown and the ability to predict its occurrence is crucial to efforts to improve current aircraft design and performance in flight at high angles of attack.

The phenomenon of vortex breakdown was observed for the first time by Peckham and Atkinson[1] in their experimental investigation of flow over delta wings. Due to its importance in the aerodynamic behavior of delta wings, the phenomenon of vortex breakdown was studied extensively in both experimental and theoretical investigations. Two types of breakdown, namely bubble–type and spiral–type, have been observed for flows over delta wings, depending on the angle of attack and wing sweep angle. Vortex shedding, adverse pressure gradients at the trailing edge and the three–dimensional flow character complicate the study of vortex breakdown over delta wings. Therefore, many of the early experimental investigations on vortex breakdown were done for axisymmetric swirling flows confined in cylindrical tubes. Various types of vortex breakdown observed for axisymmetric swirling flows are described in Ref. 2. Investigations on axisymmetric flows helped to study vortex breakdown in isolation, and enabled researchers to gain insight into the phenomenon and set criteria for the occurrence of the different types of vortex breakdown.

The structure of the vortical flow field and the effect of vortex breakdown on the three–dimensional flow over delta wings was the subject of several recent experimental investigations (cf. Refs. 3–7). Various flow regimes ranging from incompressible to high speed compressible flow were investigated. Different sweep angle wings were examined, and bubble or spiral vortex breakdown was identified depending on the angle of attack. The flow over delta wings was also studied recently by numerical solution of the Navier–Stokes equations, e.g., Refs. 8–11. The results of these numerical investigations were in good agreement

* Adjunct Research Professor, Department of Aeronautics, Naval Postgraduate School Monterey California. Member AIAA.

† Special Assistant for High Alpha Technology, Fluid Dynamics Division. Associate Fellow AIAA.

with experimental measurements, and both bubble–and spiral–type breakdown was observed.

The objective of the present numerical study is to investigate in detail the leeward–side flowfield over delta wings. The influence of grid resolution and turbulence modeling on the accuracy of the solution and the prediction of the leeward–side flow characteristics is addressed first. The leeward–side flow structure and the vortex breakdown is investigated for different angles of incidence. Finally, the effects of variation of sweep angle and free–stream speed on the flowfield and the lifting characteristics are examined.

Computational Method

Governing Equations

The thin–layer compressible Navier–Stokes equations were used to obtain the numerical solution. The strong conservation–law form of the governing equations for a curvilinear coordinate system (ξ, η, ζ) along the axial, circumferential, and normal direction respectively, is as follows

$$\partial_t \hat{\mathbf{Q}} + \partial_\xi \hat{\mathbf{F}} + \partial_\eta \hat{\mathbf{G}} + \partial_\zeta \hat{\mathbf{H}} = Re^{-1} \partial_\zeta \hat{\mathbf{S}} \qquad (1)$$

where $\hat{\mathbf{Q}}, \hat{\mathbf{F}}, \hat{\mathbf{G}}, \hat{\mathbf{H}}$ are

$$\hat{\mathbf{Q}} = \frac{1}{J}\begin{pmatrix} \rho \\ \rho u \\ \rho v \\ \rho w \\ e \end{pmatrix}, \qquad \hat{\mathbf{F}} = \frac{1}{J}\begin{pmatrix} \rho U \\ \rho u U + \xi_x p \\ \rho v U + \xi_y p \\ \rho w U + \xi_z p \\ (e+p)U - \xi_t p \end{pmatrix}$$

$$\hat{\mathbf{G}} = \frac{1}{J}\begin{pmatrix} \rho V \\ \rho u V + \eta_x p \\ \rho v V + \eta_y p \\ \rho w V + \eta_z p \\ (e+p)V - \eta_t p \end{pmatrix}, \quad \hat{\mathbf{H}} = \frac{1}{J}\begin{pmatrix} \rho W \\ \rho u W + \zeta_x p \\ \rho v W + \zeta_y p \\ \rho w W + \zeta_z p \\ (e+p)W - \zeta_t p \end{pmatrix}$$

$$\hat{\mathbf{S}} = \frac{1}{J}\begin{pmatrix} 0 \\ \mu m_1 u_\zeta + (\mu/3) m_2 \zeta_x \\ \mu m_1 v_\zeta + (\mu/3) m_2 \zeta_y \\ \mu m_1 w_\zeta + (\mu/3) m_2 \zeta_z \\ \mu m_1 m_3 + (\mu/3) m_2 + (\zeta_x u + \zeta_y v + \zeta_z w) \end{pmatrix}$$

Here

$$m_1 = \zeta_x^2 + \zeta_y^2 + \zeta_z^2$$

$$m_2 = \zeta_x u_\zeta + \zeta_y v_\zeta + \zeta_z w_\zeta$$

$$m_3 = (u^2 + v^2 + w^2)/2 + \kappa Pr^{-1} \left(\frac{\partial a^2}{\partial \zeta}\right)$$

and U, V, and W are the contravariant velocity components given by

$$U = u\xi_x + v\xi_y + w\xi_z + \xi_t$$

$$V = u\eta_x + v\eta_y + w\eta_z + \eta_t$$

$$W = u\zeta_x + v\zeta_y + w\zeta_z + \zeta_t$$

In the above equations all geometrical dimensions are normalized with the wing–root chord length; ρ is the density normalized with the free–stream density ρ_∞; u, v, and w are the Cartesian velocity components of the physical domain normalized with the free–stream speed of sound a_∞; e is the total energy per unit volume normalized with $\rho_\infty a_\infty^2$; and Pr is the Prandtl number. The pressure is related to density and total energy through the equation of state for an ideal gas, $p = (\gamma - 1)\left[e - \rho(u^2 + v^2 + w^2)/2\right]$.

Numerical Implementation

The numerical integration is performed using a partially flux–split numerical scheme[12]. The upwinding is performed in the main flow direction with flux–vector splitting, and central differencing is used in the other two spatial directions. The resulting two–factored algorithm is:

$$\begin{aligned} &\left[I + h\delta_\xi^b (A^+)^n + h\delta_\zeta C^n - hRe^{-1}\bar{\delta}_\zeta J^{-1} M^n J - D_{i|\zeta}\right] \\ &\times \left[I + h\delta_\xi^f (A^-)^n + h\delta_\eta B^n - D_{i|\eta}\right]\Delta q^n = \\ &- \Delta t\{\delta_\xi^b\left[(F^+)^n - F_\infty^n\right] + \delta_\xi^f\left[(F^-)^n - F_\infty^n\right] \\ &+ \delta_\eta(G^n - G_\infty) + \delta_\zeta(H^n - H_\infty) \\ &+ Re^{-1}\delta_\zeta(S^n - S_\infty)\} - D_e(q^n - q_\infty) \end{aligned} \qquad (2)$$

In Eq. (2) D_e are the explicit dissipation terms that are used along the directions where central differencing is employed, and D_i are the implicit dissipation terms that are added for numerical stability. The dissipation terms used are a combination of second–order and fourth–order terms. The fourth–order terms provide background damping of the high frequency modes. The second–order terms are used to control the oscillation in the neighborhood of shock waves, and are turned on when strong pressure gradients are sensed in the flow. The implicit and explicit dissipation terms are computed as suggested in Ref. 13.

Computations for both laminar and turbulent flow were carried out. For the laminar flow cases the viscosity coefficient was obtained from the Sutherland law. For the turbulent flow cases the Baldwin-Lomax eddy viscosity model[14] and a model with the modifications suggested by Degani and Schiff[15] for the computation of separated vortical flows were used. The higher Reynolds number flows where the flow over the delta wing is expected to be mostly turbulent were considered fully turbulent over the entire body, and no modeling of transition was attempted.

Solutions were obtained on spherical grid topologies. A sample spherical grid configuration employed for the computations of the 63° sweep delta wing is shown in Fig. 1. The grid boundaries were placed 2 to 2.5 root chord lengths away from the wing surface, and sufficient clustering was used in the normal direction to enable capturing of the viscous layers. Solutions were also computed with embedded grids using the Chimera[16] scheme, which enables solutions with several overlapping grids. The modifications of the axially flux–split algorithm of Eq. (2) and the dissipation operators required for the application of the Chimera scheme are discussed in Ref. 17. In the embedded grid technique the region of the overall computational grid, referred to as the global grid, in which higher resolution is required is identified. A finer grid is obtained in this region by interpolation of the global grid along one or all three coordinate directions. The resulting grid is

called an embedded grid. The crossection view shown in Fig. 2 shows both the global and the fine embedded grid. The embedded grid region includes the leeward side flow field and small region surrounding the wing leading edge. The global and embedded grids overlap at each interface. The governing equations are solved independently for each grid, and the communication between the two grids is obtained by the exchange of information at the boundaries. The flow quantities are interpolated linearly in order to transfer boundary data from the global coarser grid to the embedded grid.

Results for the 75° Sweep Delta Wing

The flow conditions of the computation were kept fixed, and matched the experimental conditions of Ref. 3. The experimental Mach number was $M_\infty = 0.3$ and the Reynolds number, based on the root chord length was $Re_c = 1 \times 10^6$. Most of the solutions were computed as laminar, because for this Reynolds number the experimental flow is mostly laminar, with the effects of transition and turbulence affecting only the regions close to the trailing edge. The effect of turbulence modeling on the computed solutions was investigated both for flows without vortex breakdown and flows exhibiting vortex breakdown.

The effect of variation of angle of attack on the leeward side flow characteristics was investigated with the solutions over the 75° sweep delta wing. Solutions were obtained at several angles of attack ranging from $\alpha = 20.5°$ to $\alpha = 55°$. The range of angles of attack studied can be divided into three flow regimes. These are: a regime having a stable quasi–conical pair of leading edge vortices, a regime where the leading edge vortices suffer a bubble–type vortex breakdown, and a regime where the leading edge vortices suffer a spiral–type vortex breakdown. The effect of grid resolution and grid embedding on the prediction of the leeward side flow characteristics for flows at moderate angles of attack where no breakdown is observed is presented first.

Embedded Grid Solutions

Embedded–grid solutions were obtained for $\alpha = 20.5°$, where detailed experimental data from Ref. 3 are available. At this angle of attack the leading–edge vortices formed by the inward spiraling of the vortex sheet from the leading edge are stable and quasi–conical. In Ref. 18 an extensive study of the numerical factors influencing the accuracy of the computation was carried out for this case. Solutions were obtained with single–block grids, zonal grids, and embedded grids. The conclusion of this study was that the zonal–grid solutions are in good agreement with the single–block solutions, and that adequate grid resolution in the circumferential direction is required for accurate solutions.

It was also found that for the embedded grids, careful selection of the region where grid refinement is performed is crucial for the sucess of the technique. The embedded grid used in Ref. 18 only included the leeward–side region extending from the wing leading edge to the leeward symmetry plane. As a result of the jump in grid resolution in the leading–edge region, discrepancies appeared between the leeward–side flow characteristics predicted by the single–block and embedded–grid solutions. The present embedded grid provides improved grid resolution both on the leeward side and on a small part of the windward side close to the leading edge. The coarse global grid is a $56 \times 54 \times 35$ point grid, and the embedded fine grid is obtained by interpolation of the coarse grid in all three directions. The embedded grid region starts close to the apex, and extends axially downstream to the trailing edge. In the circumferential direction (see Fig. 2) the refined zone starts on the windward side of the wing close to the leading edge, wraps around the leading edge, and extends to the leeward plane of symmetry. In the normal direction the embedded grid starts from the body surface and extends far enough outward to avoid placing of the outer boundary of the embedded grid in regions where large flow gradients occur.

The leeward–side surface pressure coefficient for the axial location x/c = 0.5 computed with the embedded grid is compared in Fig. 3 with the measurements of Ref. 3, a fine single–block grid solution, and the solution obtained with the previous embedded grid. The single–block solution was obtained on a fine, $112 \times 105 \times 70$ point, grid which provides the same grid resolution as the embedded grids on the leeward side. The previous embedded–grid solution is generally in good agreement with the single–block solution and the experimental measurements, although a small discrepancy between the two numerical solutions is seen for $y/y_{max} \approx 0.7$ in the region between the two suction peaks. Extending the embedded grid to include the wing leading edge improves the agreement between the single–block and embedded–grid solutions in this region.

The off–surface leeward–side pressure field in a cross-flow plane at x/c = 0.5, computed using the single–block grid, the current (circumferentially extended) embedded grid, and the previous embedded grid are shown in Figs. 4a, 4b, and 4c, respectively. The single–block–grid solution and the current embedded–grid solutions are in very close agreement, both in magnitude of the pressure in the vortex core and in details of the flowfield in the vicinity of the wing leading edge. In contrast, the previous embedded–grid solution (Fig. 4c) shows small differences in the location of the vortex core and slight differences in pressure in the vicinity of the leading edge. It can be also seen in Figs. 4a–c that the primary vortex is located at $y/y_{max} \approx 0.7$, above the area where the discrepancies in surface pressure are observed in Fig. 3. Thus, differences in the surface pressures appear to be caused by the differences in the strength of the primary vortices, which in turn are caused by the differences in circumferential resolution of the grids. This again confirms the necessity of using sufficient grid resolution in regions of high flow gradients in order to obtain accurate numerical solutions.

Effect of Turbulence Modeling

The experimental[3] leeward–side surface oil–flow pattern for $\alpha = 20.5°$ is shown schematically in Fig. 5a. Both the secondary separation line and the tertiary separation line (occurring between the secondary separation and the primary separation at the wing leading edge) can be observed. In addition, lines of attachment are observed on the wing leeward plane of symmetry and between each pair of lines of separation. At the Reynolds number of the experiment ($Re_c = 1 \times 10^6$) the flow appears to be mostly laminar. Outboard displacement of the separation and attachment lines, which characterizes transition to turbulence of the surface flow, is not evident except in the region

close to the wing trailing edge. However, the flow in this region may be also affected by the presence of the trailing edge and the wake. The influence of the wake on the surface flow can be seen in the computed laminar surface–flow pattern of Fig. 5b. The computed surface flow pattern shows a small region of reversed flow near the trailing edge between the secondary and tertiary separation lines.

The effect of turbulence modeling on the computed flow was investigated numerically for this case. Computations were made using the Baldwin–Lomax[14] algebraic eddy–viscosity model with the modifications suggested by Degani and Schiff[15] to account for crossflow separation, using a $56 \times 54 \times 70$ point grid. Although the experimental flow is believed to be mostly laminar, the flow was assumed to be fully turbulent in these computations. The computed turbulent surface pressure distributions at x/c = 0.5 is shown in Fig. 6, and is compared to the experimental measurements, and to the laminar solution obtained with the same grid. In contrast to high–incidence flow over bodies of revolution, where there is strong interaction between the strength of the primary vortex and the location of the primary crossflow separation line, for sharp–edged delta wings primary crossflow separation occurs at the wing leading edge. In this case the main effect of turbulence modeling is to increase the amount of vorticity in the vortex feeding sheets, and thus to increase the strength of the primary and the secondary vortices. This results in higher suction peaks in the vicinity of the vortices (see Fig. 6). Also, the secondary separation line occurred further outboard in the turbulent computation, in agreement with the experimentally observed trend. As a result, the turbulent surface suction peaks are displaced outboard, closer to the wing leading edge.

The effect of turbulence modeling on the prediction of flowfields at higher incidence ($\alpha = 40^o$) where vortex breakdown is observed was also investigated. The surface pressure coefficient for the axial locations x/c = 0.3 and x/c = 0.5, obtained by two laminar solutions of different grid densities, and turbulent solutions obtained using both the turbulence models of Refs. 14 and Ref. 15 are shown in Figs. 7a and 7b. The laminar solutions, computed with a $56 \times 105 \times 70$ point and a $56 \times 54 \times 70$ point grid, are in reasonable agreement at both axial locations. Some discrepancies are observed close to the leading edge, where the circumferential grid resolution plays an important role on the accuracy of the solution. For the axial location x/c = 0.3 (Fig. 7a), the trends of the turbulent solutions, obtained on a $56 \times 54 \times 70$ grid, are the same as in the $\alpha = 20.5^o$ case. Higher suction peaks are observed in the vicinity of the vortices. However, at the downstream station (x/c = 0.5) the changes in the turbulent solutions compared to the laminar solutions are more pronounced. This behavior can be readily explained by examining the leeward–side flowfield structure. Figure 8 shows the leading–edge vortex and the breakdown region for the laminar solution (Fig. 8a), the solution computed with the modified turbulence model of Ref. 15 (Fig. 8b), and the solution computed with the turbulence model of Ref. 14 (Fig. 8c). In the laminar solution vortex breakdown occurs downstream of x/c = 0.5. However, both turbulent solutions exhibit vortex breakdown occurring upstream of x/c = 0.5. Thus, the lower suction peaks observed in the turbulent case in Fig. 7b are caused by the differences in bursting point location. The bursting point location and the extent of the vortex breakdown region are seen to be sensitive to the turbulence modeling.

Effect of Increasing Incidence

Computed values of the lift coefficient for the range of angles of attack investigated are shown in Fig. 9, together with the experimental measurements of Refs. 3 and 19. The experimental conditions of Ref. 3 were the same as in the present computation. The measurements of Ref. 19 were done for almost incompressible flow having approximately the same Reynolds number. The computed lift coefficients are in good agreement with the measurements of Ref. 3 over the entire range of measured angles of attack. The drop–off in lift for $\alpha \geq 32^o$, caused by the onset and development of vortex breakdown, is closely predicted. As expected, the measured low speed lift curve (Ref. 19) is higher than that of Ref. 3, but exhibits a similar trend, including the drop–off in lift for $\alpha \geq 35^o$. Thus, the computed lift values for $\alpha = 50^o$ and 55^o seem reasonable. The turbulent computation at $\alpha = 20.5^o$ gave a slightly higher lift coefficient value than the laminar result because it predicted slightly higher suction peak values. In contrast, the turbulent computation for $\alpha = 40^o$ predicted a lower value of the lift coefficient because vortex breakdown was predicted further upstream and the breakdown region was larger.

The solutions for angles of attack $\alpha = 50^o$ and $\alpha = 55^o$ showed spiral–type vortex breakdown and did not reach a steady state. For these cases a single value of the lift coefficient was not obtained. The time–history of the computed lift coefficient for $\alpha = 50^o$ is shown in Fig. 10. Flow moving with free–stream velocity would require a nondimensional time of $[T] \approx 3.3$ to travel a distance equal to the root chord. In Fig. 10, the initial behavior of the flow $0 \leq [T] \leq 10$ is not shown. The variation of the lift for $10 \leq [T] \leq 20$ is small and relatively slow.

Structure of Vortex Breakdown

A bubble–type vortex breakdown was first observed at the wing trailing edge in the solutions computed for $\alpha = 32^o$. This is in agreement with an experiment (Ref. 7) in which vortex breakdown was first observed for a similar configuration at $\alpha = 32^o$. For cases computed at angles of attack between $\alpha = 32^o$ and $\alpha = 40^o$ the same bubble–type breakdown was observed in the solution. The location of the vortex burst point moves progressively forward on the wing with increase in angle of attack. As the wing incidence is increased further, beyond a critical angle of attack, a change in the vortex breakdown type from steady bubble–type to an unsteady spiral–type occurs. This has been previously observed experimentally (Refs. 4, 20), and in computations (Ref. 8) for flow over a strake–delta wing. The present computations for flow over the delta wing at $\alpha = 50^o$ and 55^o exhibit spiral–type, unsteady vortex breakdown.

The general leeward–side flow characteristics for flow without vortex breakdown, for flow with bubble type of vortex breakdown, and for flow with spiral–type vortex breakdown are demonstrated in Fig. 11. The flowfield structure for flow without vortex breakdown ($\alpha = 30^o$) is shown in Fig. 11a with streamlines originating from the wing apex. The leading–edge vortices remain quasi–conical and stable over the body, deflecting slightly at the trailing edge and turning toward the free steam. For $\alpha = 35^o$ (Fig. 11b) bubble–type breakdown is observed with the breakdown point located above the wing at x/c ≈ 0.8. The bubble size and breakdown location can both be seen

in Fig. 11b. The initially quasi–conical structure of the primary vortex is illustrated by the streamlines spiraling closely around each other. Downstream of breakdown a sudden expansion of the vortex is observed. For $\alpha = 50°$ (Fig. 11c) and $\alpha = 55°$ (Fig. 11d) unsteady spiral–type vortex breakdown was identified. As mentioned above, at $\alpha = 50°$ and $55°$ the computed solution does not reach a steady state. The flow quantities inside the vortex breakdown region showed fairly large variation. Thus, the spiral breakdown structures shown in Figs. 11c and 11d are "snapshots" of the unsteady flow, indicated by instantaneous streamlines originating from the apex region. The breakdown point for $\alpha = 50°$ is located at $x/c \approx 0.4$. In comparison with the case at $\alpha = 35°$, the breakdown region is much larger. Similarly, at $\alpha = 55°$ the breakdown point location is further upstream, $x/c \approx 0.3$, and the breakdown region is more extensive.

The spiral vortex structure obtained for $\alpha = 50°$ is shown in detail with "snapshots" of the computed pressure field. The approximate vortex core location is shown in Fig. 12 by the pressure field contours in crossflow planes at different axial locations x/c = 0.6, 0.8 and 1.0. In this figure both the spanwise and the vertical coordinates are normalized with the local span. Thus, a quasi–conical leading–edge vortex structure would be located at approximately the same normalized spanwise and vertical location. This is not the case at $\alpha = 50°$. The displacement and spiraling of the vortex core can be clearly observed in Fig. 12. The spiraling of the vortex can also be seen in Fig. 13, which shows pressure contours in a longitudinal plane passing approximately through the vortex core. The location of the burst point remained fixed as the computation was continued in time, and the flowfield quantities did not vary at locations outside the breakdown region. The variation of the velocity components for a fixed location within the vortex breakdown region is shown in Fig. 14. The time–variation of the velocity components is relatively slow, similar to the variations in lift (Fig. 10).

Results for the 63° Sweep Delta Wing

To assess the effect that variation of wing leading–edge sweep angle has on the flow structure, solutions were computed for the flow over a 63° sweep delta wing. Experimental data for this wing geometry were reported in Ref. 6. Solutions were computed for two cases matching those of the experiment, a subsonic case at $M_\infty = 0.2, \alpha = 21°, Re_c = 3.5 \times 10^6$ and a transonic case at $M_\infty = 0.8, \alpha = 21.8°, Re_c = 10 \times 10^6$. Solutions were obtained using a $58 \times 54 \times 70$ point spherical grid. For these high flow Reynolds numbers it is believed that laminar and transitional effects would be limited to a small region near the wing apex. Thus, the computed flows were considered to be fully turbulent, and the turbulent model of Ref. 15 was used.

The computed spanwise surface pressure distribution for the subsonic case is shown in Fig. 15 at x/c = 0.5, together with the experimental data. It is observed (compare Figs. 3 and 15), that at similar angles of attack the 63° sweep wing has a higher primary suction peak than the 75° sweep wing. Although the Reynolds number differs between the two cases, for sharp–edged delta wings it is expected that the Reynolds number effects are small. It was demonstrated (see Fig. 6) that turbulent solutions yield slightly higher surface pressure, but the doubling of the suction peak values observed in Fig. 15 is caused primarily by the decrease of the sweep angle. It is well known[21] that decrease of the sweep angle results in higher lift values and earlier occurrence of breakdown as the angle of attack increases. For $\alpha = 21°$, no vortex breakdown was found over the wing surface. Although experiments[6] reported breakdown in the wake region, the computational grid in this region was too coarse to enable capturing of the small size vortex breakdown.

The surface pressure distribution at x/c = 0.5 for the transonic flow at $M_\infty = 0.8, \alpha = 21.8°$ is compared with the measurements in Fig. 16. The well known reduction in vortex lift with increasing Mach number observed in the solution (compare Figs. 16 and 15). The suction peak due to the primary vortex is reduced considerably for the higher Mach number case. The solution shows vortex breakdown above the wing for $x/c \geq 0.5$. This breakdown is shown in Fig. 17 with streamlines released from the wing apex.

The analogous computed surface–flow pattern is compared with the experimentally obtained oil–flow pattern in Fig. 18. These indicate an outboard shift of the secondary separation line for $x/c \geq 0.5$, caused by the vortex breakdown. The computed surface flow pattern follows the trends of the experimental oil–flow pattern, but the outboard shift of the surface streamlines occurs further upstream in the computation. These differences are probably caused by the different bursting point location and extent of breakdown region predicted by the numerical solution.

For transonic flow over delta wings at incidence, the leeward–side flow can reach supersonic speeds. This was observed in the solution for $M_\infty = 0.8, \alpha = 21.8°$. The supersonic region above the primary vortex and the curved shock formed inboard of this region are shown in Fig. 19 with the Mach contours in a crossflow plane. The supersonic region above the primary vortex is included in the area marked with a thick line. The shock location, marked with a dashed line, is in agreement with the shock location identified by the experimental investigation of Ref. 6.

Summary

Flows over a 75° sweep and a 63° sweep delta wing were investigated. Solutions obtained with an embedded grid technique were in good agreement with the experimental measurements and the solutions computed on a single–block fine grid. The effect of turbulence modeling was investigated for flows with and without vortex breakdown. The prediction of the location of the bursting point and the size of the breakdown region was found to be sensitive to turbulence modeling. The lift characteristics were predicted satisfactorily by the numerical solution, and the results were in good agreement with the measured lift values. As the angle of attack was increased, a progression from no breakdown to steady bubble–type breakdown to unsteady spiral–type breakdown was seen in the computed results. Decrease of the sweep angle resulted in increased suction peaks at the leeward side. For high–speed flow, supersonic flow regions formed over the primary vortices, and a curved shock formed inboard normal to the primary vortex.

References

[1]Peckham, D. H. and Atkinson, S. A., "Preliminary Results of Low Speed Wind Tunnel Tests on a Gothic Wing of Aspect Ratio 1.," *Aeronaut. Res. Counc.*, CP 508, 1957, Paper 16.

[2]Faler, J. H. and Leibovitch, S., "Disrupted States of Vortex Flow and Vortex Breakdown," *Physics of Fluids*, Vol. 20, 1977, pp. 1385–1400.

[3]Hummel, D., "On the Vortex Formation over a Slender Wing at Large Angles of Incidence," AGARD–CP–247, 15, Norway, Oct. 1978.

[4]Payne, F. M. and Nelson, R. C., "An Experimental Investigation of Vortex Breakdown on Delta Wings," Vortex Flow Aerodyanmics, NASA CP–2416, 1985, pp. 135–161.

[5]Kjelgaard, O. and Sellers, W. L., "Detailed Flowfield Measurements Over a 75° Swept Delta Wing for Code Validation," AGARD Symposium on Validation of CFD, May 2–5, 1988, Lisbon, Portugal.

[6]Schrader, K. F., Reynolds, G. A., and Novak, C. J., "Effects of Mach Number And Reynolds Number on Leading–Edge Vortices at High Angle–of–Attack," AIAA Paper 88–0372, 26th Aerospace Science Meeting, Jan. 11–14, Reno, Nevada, 1988.

[7]Magness, C., Robinson, O., and Rockwell, D., "Control of Leading–Edge Vortices on a Delta Wing," AIAA Paper 89–0999, March 1989.

[8]Fujii, K. and Schiff, L. B., "Numerical Simulation of Vortical Flows over Strake–Delta Wing," *AIAA J.*, Vol. 27, Sept. 1989, pp. 1153–1162.

[9]Thomas J. L., Taylor, S. L., and Anderson, W. K., "Navier–Stokes Computations of Vortical Flows over Low Aspect Ratio Wings," AIAA Paper 87–0207, 25th Aerospace Science Meeting, Reno, Nevada, Jan. 1987.

[10]Kandil, O. A. and Chuang, A. H., "Unsteady Vortex–Dominated Flows around Maneuvering Wings over a Wide Range of Mach Numbers," AIAA Paper 88–0317, 26th Aerospace Sciences Meeting, Reno, Nevada, Jan. 1988.

[11]Hsu, C. H. and Liu, C. H., "Prediction of Vortical Flows on Wings Using Incompressible Navier–Stokes Equations," Third International Congress of Fluid Mechanics, Cairo, Egypt, Jan. 1990.

[12]Ying, S. X., Steger, J. L., Schiff, L. B., and Baganoff, D., "Numerical Simulation of Unsteady, Viscous High–Angle–of–Attack Flows Using a Partially Flux–Split Algorithm," AIAA Paper 86–2179, 1986.

[13]Pulliam, T. H., "Artificial Dissipation Models for the Euler Equations," *AIAA J.*, Vol. 24, Dec. 1986, pp. 1931–1940.

[14]Baldwin, B. S. and Lomax, H., "Thin Layer Approximation and Algebraic Model for Separated Turbulent Flows," AIAA Paper 78–275, 1978.

[15]Degani, D., and Schiff, L. B., "Computation of Turbulent Supersonic Flows around Pointed Bodies having Crossflow Separation," *Journal of Comp. Physics*, Vol. 66, No. 1, Sept. 1986, pp. 173–196.

[16]Benek, J. A., Buning, P. G., and Steger, J. L., "A 3D Chimera Grid Embedding Technique," AIAA Paper 85–1523, 7th Computational Fluid Dynamics Conference, Cincinnati, Ohio, July 1985.

[17]Buning, P. G., Chiu, I. T., Obayashi, S., Rizk, Y. M., and Steger, J. L., "Numerical Simulation of the Integrated Space Shuttle Vehicle in Ascent," AIAA Paper 88–4359–CP, 1988.

[18]Ekaterinaris, J. A. and Schiff, L. B., "Vortical Flows over Delta Wings and Numerical Prediction of Vortex Breakdown," AIAA Paper 90–0102, 28th Aerospace Sciences. Meeting, Jan. 1990.

[19]Wentz, W. H., and Kohlman, D. L., "Vortex Breakdown on Slender Sharp–Edged Delta Wings," *Journal of Aircraft*, Vol. 8, No. 3, 1971, pp. 156–161.

[20]Ayoub, A. and McLachlan, B. G., "Slender Delta Wing at High Angles of Attack – a Flow Visualization Study," AIAA Paper 87–1230, AIAA 19th Fluid Dynamics Conf. Honolulu, Hawaii, June 1987.

[21]Polhamus, E. C., "Prediction of Vortex–Lift Characteristics by a Leading–Edge Suction Analogy," *Journal of Aircraft*, Vol. 8, No. 4, Apr. 1971, pp. 193–199.

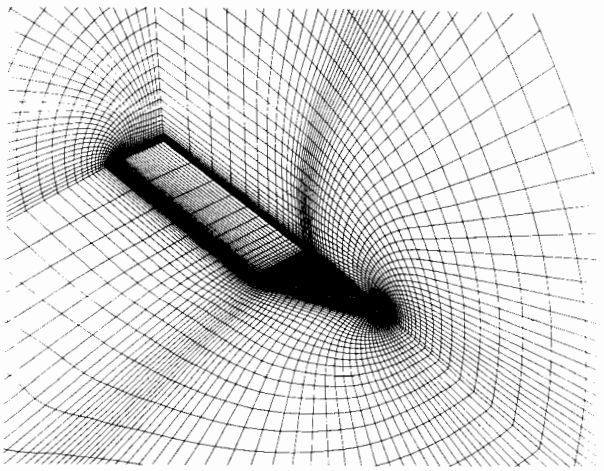

Fig. 1 Spherical grid over the 63° sweep delta wing.

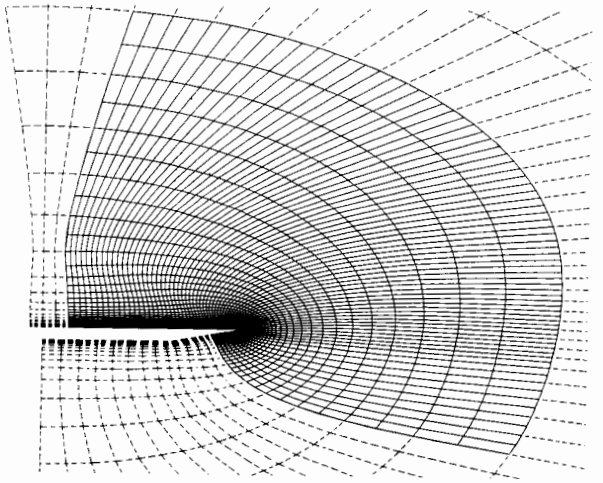

Fig. 2 Crossection view of the global (coarse), and embedded (fine) grid wrapped around the leading edge and including the vortical flow region.

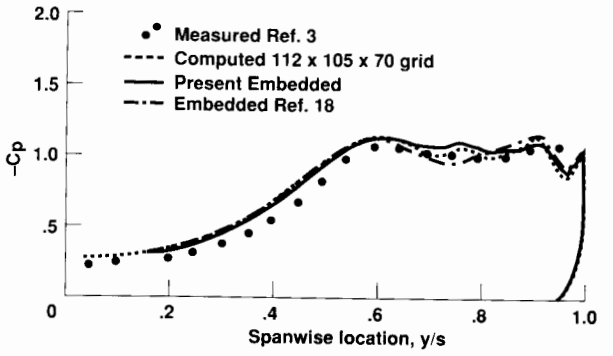

Fig. 3 Comparison of the leeward side surface pressure coefficient at x/c = 0.5 computed with single block and embedded grids: $M_\infty = 0.3, \alpha = 20.5°, Re = 1 \times 10^6$ (laminar).

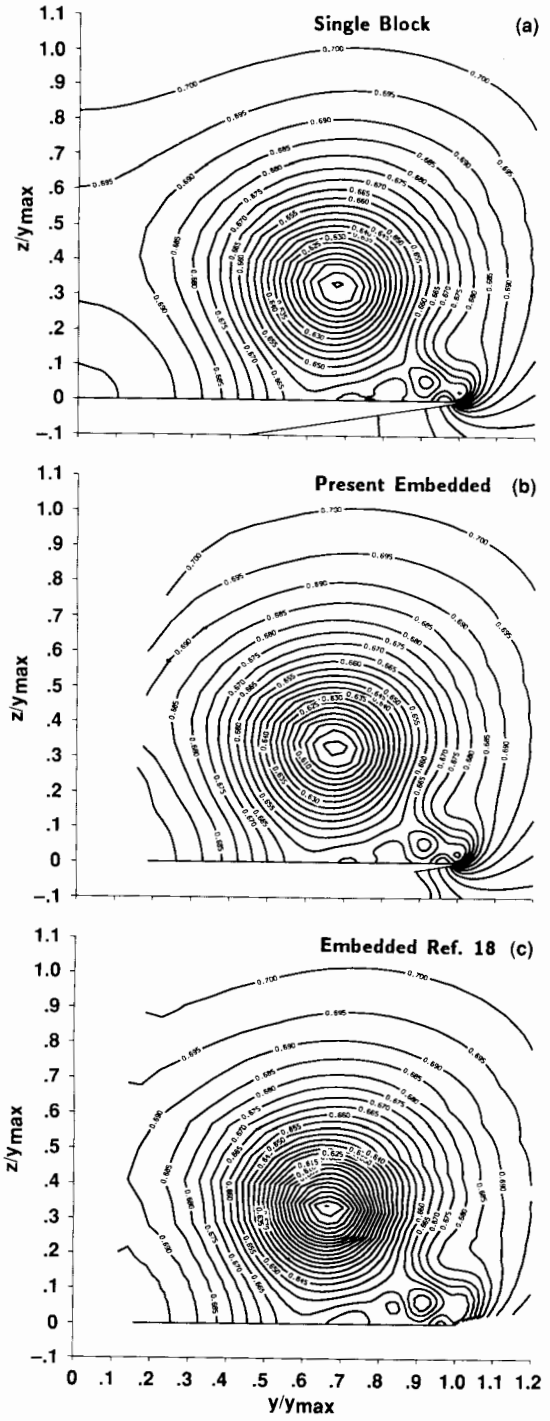

Fig. 4 Comparison of the leeward–side pressure field at x/c = 0.5 computed with single block and embedded grids: $M_\infty = 0.3, \alpha = 20.5°, Re = 1 \times 10^6$.

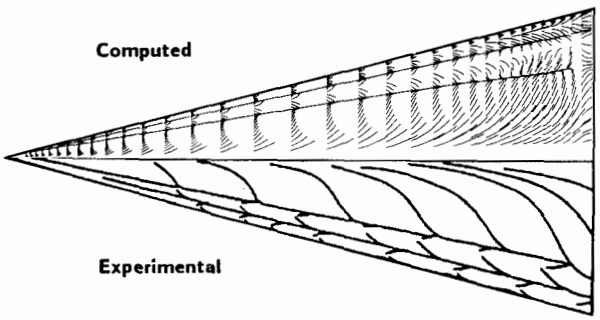

Fig. 5 Computed surface flow and experimental oil flow pattern: $M_\infty = 0.3, \alpha = 20.5°, Re = 1 \times 10^6$ (laminar).

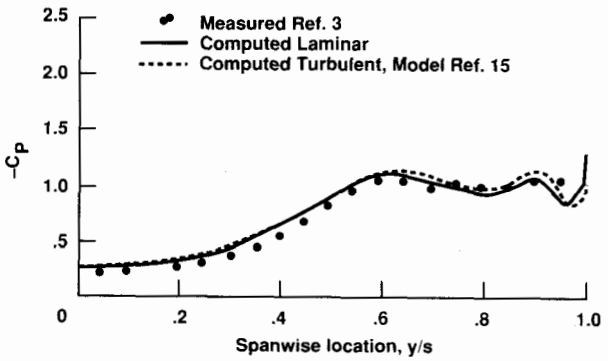

Fig. 6 Effect of turbulence modeling on the prediction of the surface pressure coefficient: $M_\infty = 0.3, \alpha = 20.5°, Re = 1 \times 10^6$.

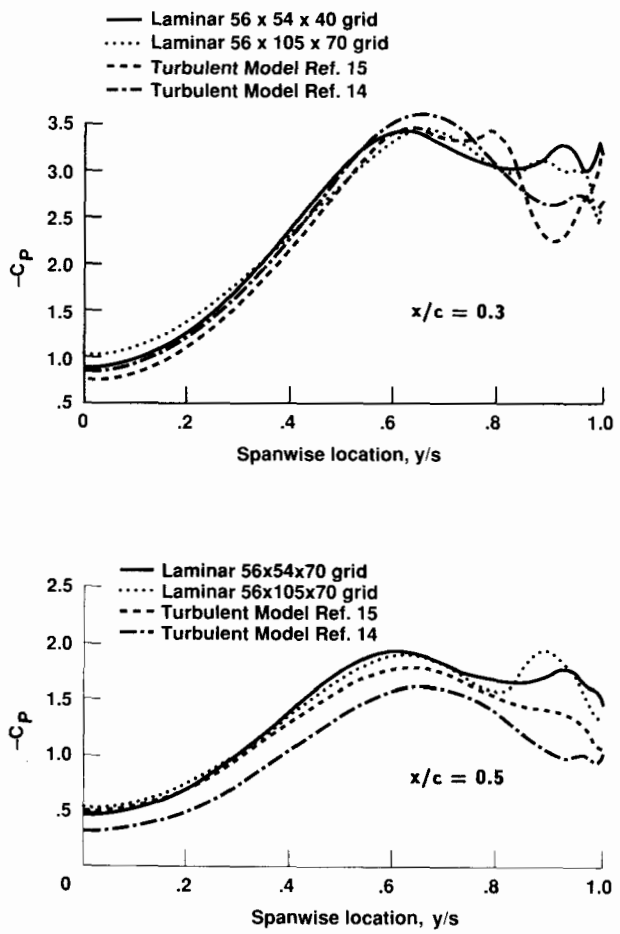

Fig. 7 Computed surface pressure distribution on the 75° sweep delta wing: $M_\infty = 0.3, \alpha = 40°, Re = 1 \times 10^6$.

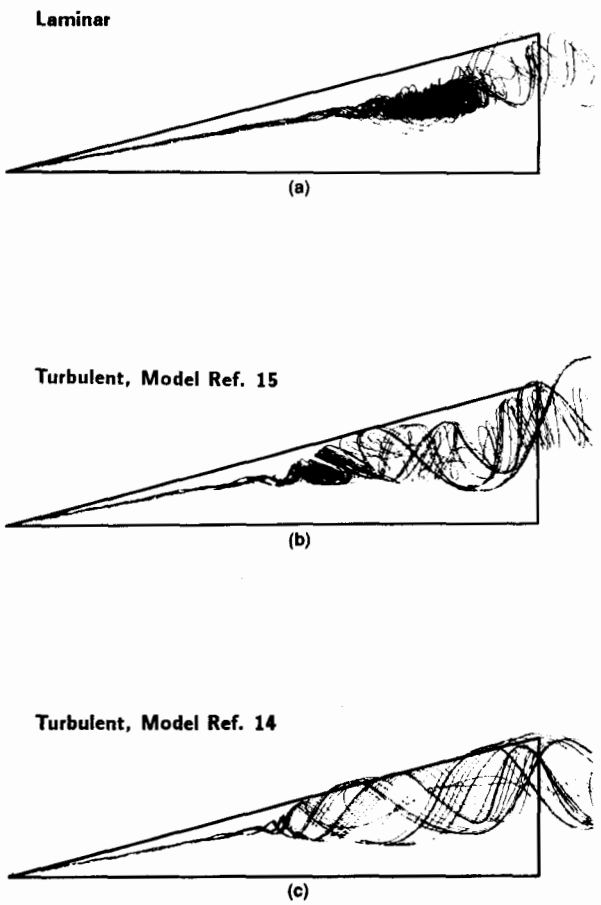

Fig. 8 Vortex breakdown location over a 75° sweep delta wing: $M_\infty = 0.3, \alpha = 40°, Re = 1 \times 10^6$.

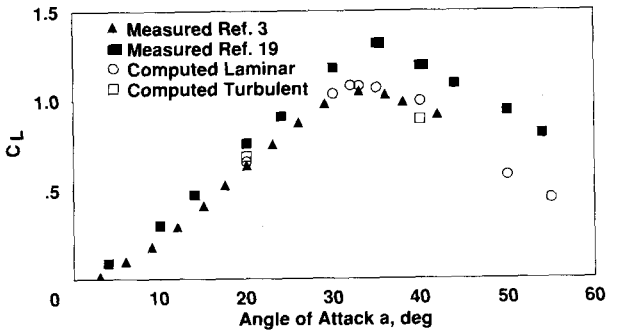

Fig. 9 Computed and measured lift coefficient at different angles of attack.

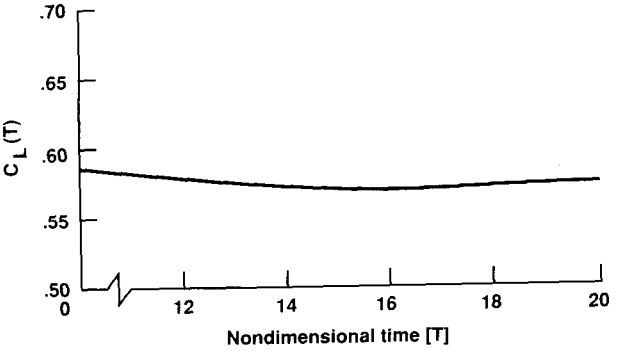

Fig. 10 Time history of the computed lift coefficient for $\alpha = 50°$: $M_\infty = 0.3, Re = 1 \times 10^6$ (laminar).

(a) $\alpha = 30°$

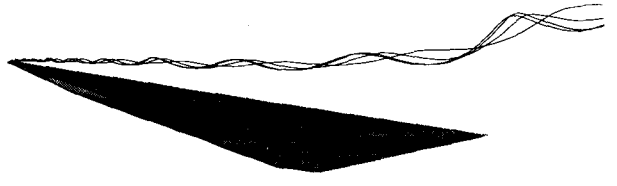

(b) $\alpha = 35°$

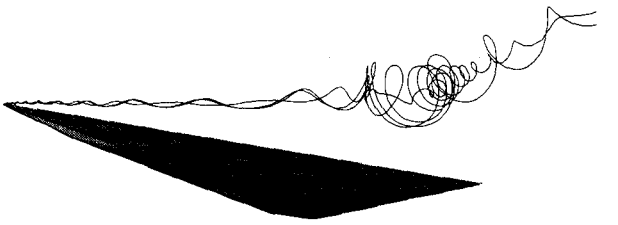

(c) $\alpha = 50°$

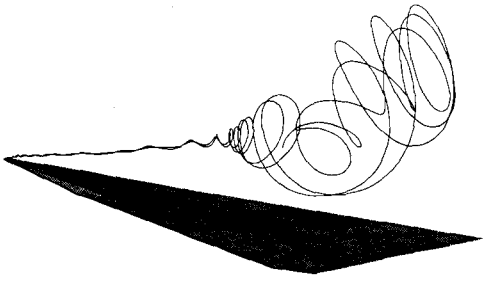

(d) $\alpha = 55°$

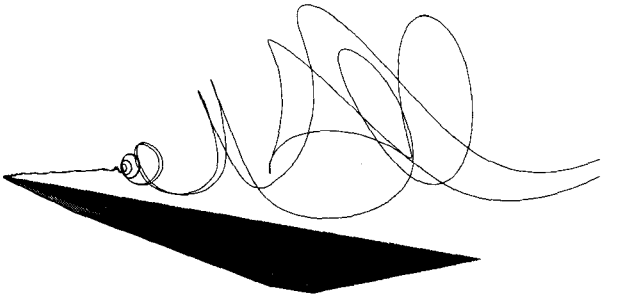

Fig. 11 Leeward–side flow structure visualized by streamlines: $M_\infty = 0.3, Re = 1 \times 10^6$ (laminar).

Fig. 11 (concluded)

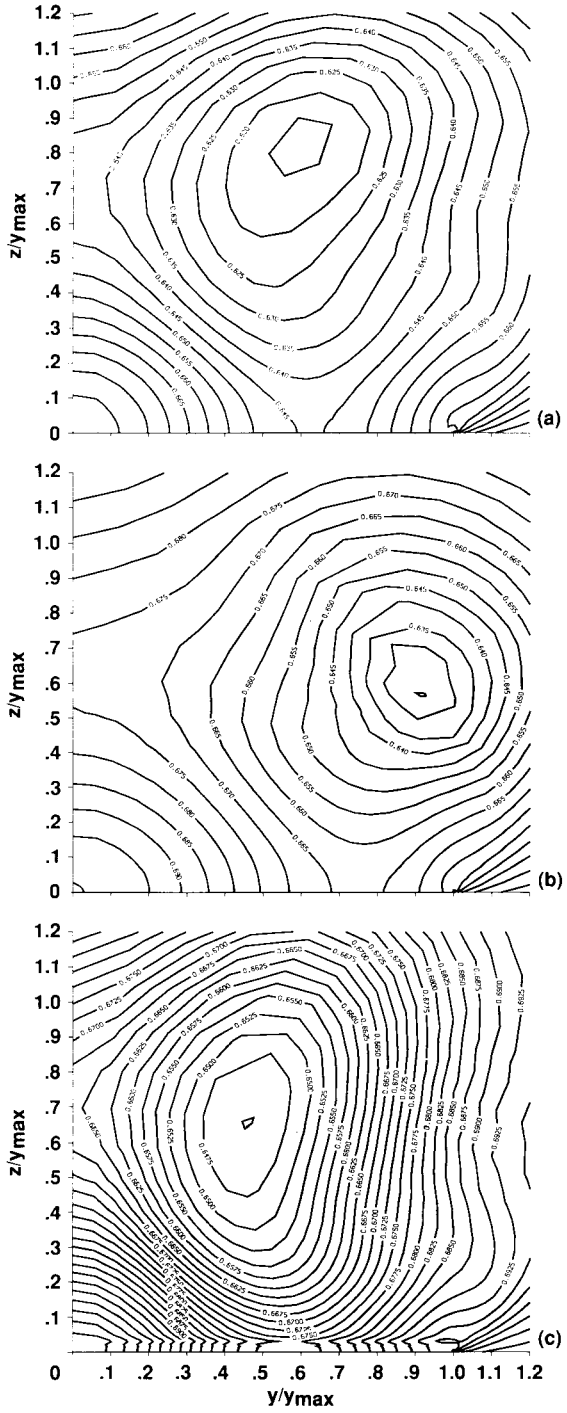

Fig. 12 Computed pressure field in crossflow planes at x/c = 0.6, 0.8 and 1.0: $M_\infty = 0.3, \alpha = 50°, Re = 1 \times 10^6$ (laminar).

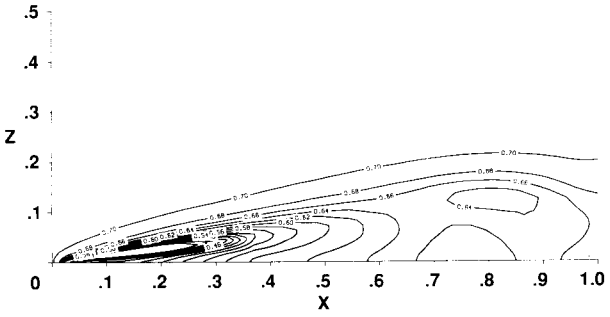

Fig. 13 Computed pressure field in a longitudinal crossection approximately through the vortex core: $M_\infty = 0.3, \alpha = 50°, Re = 1 \times 10^6$ (laminar).

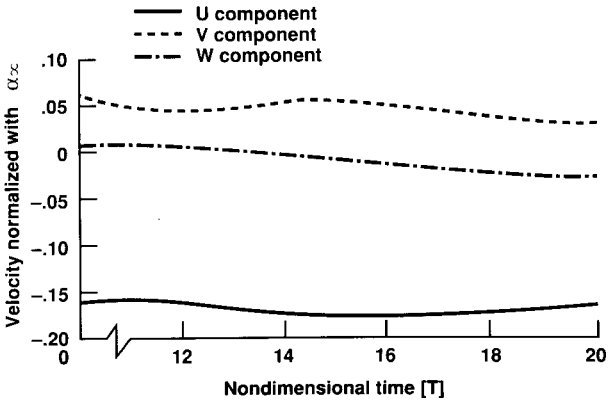

Fig. 14 Variation of the velocity components within the vortex breakdown region: $M_\infty = 0.3, \alpha = 50°, Re = 1 \times 10^6$ (laminar).